


© 2023 Optica Publishing Group. One print or electronic copy may be made for personal use only. Systematic reproduction and distribution, duplication of any material in this paper for a fee or for commercial purposes, or modifications of the content of this paper are prohibited.

link to online abstract
<https://doi.org/10.1364/boe.502022>



Time domain diffuse Raman spectroscopy using single pixel detection

ALESSANDRO BOSSI,^{1,2,*}  SANATHANA KONUGOLU VENKATA SEKAR,³  MICHELE LACERENZA,^{1,4} VALERIO GANDOLFI,¹ STEFAN ŠUŠNJAR,^{5,6} PRANAV LANKA,³  COSIMO D'ANDREA,¹  RENZO VANNA,⁷  GIANLUCA VALENTINI,^{1,7}  ANDREA FARINA,⁷  AND ANTONIO PIFFERI^{1,7} 

¹Politecnico di Milano, Department of Physics, Milan, Italy

²Politecnico di Milano, Department of Mechanics, Milan, Italy

³IPIC, Tyndall National Institute, Cork, Ireland

⁴PIONIRS s.r.l. Milano, Italy

⁵SpectraCure AB, Gasverksgatan 1, SE-222 29 Lund, Sweden

⁶Department of Physics, Lund University, P.O. Box 118, SE-221 00 Lund, Sweden

⁷CNR-Institute for Photonics and Nanotechnologies (CNR-IFN), Milan, Italy

*alessandro.bossi@polimi.it

Abstract: Diffuse Raman spectroscopy (DIRS) extends the high chemical specificity of Raman scattering to in-depth investigation of thick biological tissues. We present here a novel approach for time-domain diffuse Raman spectroscopy (TD-DIRS) based on a single-pixel detector and a digital micromirror device (DMD) within an imaging spectrometer for wavelength encoding. This overcomes the intrinsic complexity and high cost of detection arrays with ps-resolving time capability. Unlike spatially offset Raman spectroscopy (SORS) or frequency offset Raman spectroscopy (FORS), TD-DIRS exploits the time-of-flight distribution of photons to probe the depth of the Raman signal at a single wavelength with a single source-detector separation. We validated the system using a bilayer tissue-bone mimicking phantom composed of a 1 cm thick slab of silicone overlaying a calcium carbonate specimen and demonstrated a high differentiation of the two Raman signals. We reconstructed the Raman spectra of the two layers, offering the potential for improved and quantitative material analysis. Using a bilayer phantom made of porcine muscle and calcium carbonate, we proved that our system can retrieve Raman peaks even in the presence of autofluorescence typical of biomedical tissues. Overall, our novel TD-DIRS setup proposes a cost-effective and high-performance approach for in-depth Raman spectroscopy in diffusive media.

© 2023 Optica Publishing Group under the terms of the [Optica Open Access Publishing Agreement](#)

1. Introduction

Raman spectroscopy provides information on the chemical composition of materials and biological samples with no need of labelling/staining and in principle non-invasively. Raman spectroscopy was typically limited to surface probing, as in microscopy. Recently, there was a strong impetus in extending Raman applicability to sub-surface probing of diffusive materials at depth of a few cm [1], opening the way to applications in several fields, from clinical diagnostics [2–4] to cultural heritage [5,6], from food assessment [7] to quality control in pharma [8], up to security controls at airports [9,10].

Different approaches were proposed to study Raman signal in depths, such as Spatially Offset Raman Spectroscopy (SORS) [11,12], Transmittance Raman Spectroscopy (TRS) [13], Frequency Offset Raman Spectroscopy (FORS) [14], Time-Domain Diffuse Raman Spectroscopy (TD-DIRS) [15]. They all share the same quest to tackle the detection of Raman emission with photon random

migration in highly diffuse media (e.g. biological tissues in the 600-1100 nm range) and can be grouped under the general field of Diffuse Raman Spectroscopy (DIRS). Each specific approach uses a different variable to yield depth sensitivity for Raman scatterers. In particular: i) SORS exploits source-detector separation (larger distances lead to deeper penetration); ii) FORS uses the excitation wavelength (different mean penetration depths depending on the spectral variation of the absorption and the scattering coefficient); iii) TD-DIRS is based on the photon arrival time (longer lived photons have travelled deeper into the medium). Conversely, TRS does not rely on a specific parameter to achieve depth selectivity. Rather, the transmittance geometry — whenever the probed medium permits — provides almost flat sensitivity for all Raman scatterers located along the source-detector line, thus reducing the penalty of buried Raman signals. This geometry, implemented in multiple source-detectors pairs is also suitable for tomographic reconstruction, although signal paucity and sample/tissue accessibility is a great hurdle.

TD-DIRS is in principle very powerful since depth information is encoded in photon arrival time and no change in wavelength/collection distance is needed as photons can be classified based on their arrival time, while keeping the very same collection efficiency and collection geometry [15]. Moreover, illumination/collection from the very same point in the null source-detector configuration is possible, with benefits in spatial resolution, signal strength and probe handling [16]. The improved manoeuvrability of the device could prove useful in various biomedical applications, including *in-vivo* measurements and surgical procedures. The key obstacles for TD-DIRS reside in the need for a short-pulsed (10-100 ps) but narrowband (<1 nm) laser source and a parallel detector suitable to be coupled with a spectrometer to measure single-photon arrival time at multiple wavelengths with ps temporal resolution. Indeed, the detector is the key limiting factor since there is no equivalent CCD (high quantum efficiency, high fill factor, high number of pixels) for time-domain single photon measurements. Initial attempts used intensified time-gated cameras to suppress early photons by applying a programmable temporal gate window [17]. Yet, these cameras are still too noisy to extract feeble Raman signals from biological tissues. An interesting perspective was opened by the availability of a time-correlated single-photon camera, yet the limited sensitivity above 600 nm, requiring the use of a lower wavelength excitation laser that induce significant autofluorescence, and the clipping to a max count rate of 10^6 counts/s still represented an obstacle for *in vivo* measurements [15]. Arrays of Single Photons Avalanche Diodes (SPADs) are surely an interesting perspective for CMOS compatibility and on-chip integration with Time-to-Digital-Converter (TDC) electronics. At present, the fill factor is still low, and the first demonstrations have been proposed for the rejection of fluorescence photons by time-gating [18] and for Diffuse Raman yet through semi-transparent media [19].

In the present paper we propose a new approach based on compress sensing to overcome the limitations of current time-domain detectors. A single-pixel time-resolved detector is used in combination with a Digital Micromirror Device (DMD) to provide spectral sampling of the Raman signal. The signal, dispersed through a standard spectrometer, is modulated using the DMD with a 50% ON/OFF pattern sequence and conveyed to the single-pixel detector. If a proper orthonormal basis is used (e.g. the Hadamard basis) and an inverse transform is applied, the Raman spectra can be retrieved, preserving information on photon arrival time.

The paper is organised as follows. First, we describe the experimental setup and provide basic performances (e.g. spectral resolution, temporal resolution). Then, Diffuse Raman spectra obtained from a two-layered tissue-equivalent phantoms made of a scattering silicone slab on top of calcium carbonate and a slice of porcine meat on top of calcium carbonate are shown, demonstrating increasing depth sensitivity for late arriving photons. Finally, the spectra of the upper and lower layers are retrieved using an inverse reconstruction algorithm [20] based on a solution of the Diffusion Equation modified to describe diffuse Raman signals.

2. Methods

2.1. System setup

Figure 1, on the top, displays the scheme of the system setup, while, on the bottom, highlights the layout of the spectrometer, which follows the design proposed in Ref. [21] to exploit a DMD for single-pixel measurements. The illumination source was a custom made tunable Ti:Sa laser with active mode-locking using acousto-optical modulation [22]. The laser was pumped at 532 nm by the second harmonic of an Nd:YAG laser, yielding a train of pulses at a repetition rate of 100 MHz, adjustable pulse width from 50 up to 500 ps, and tunable in the 680-880 nm range with a spectral width <0.1 nm [23]. A small fraction of the laser beam was diverted to a detector by a beamsplitter to synchronise a Time-Correlated Single-Photon Counting Board (TCSPC) with the laser repetition rate.

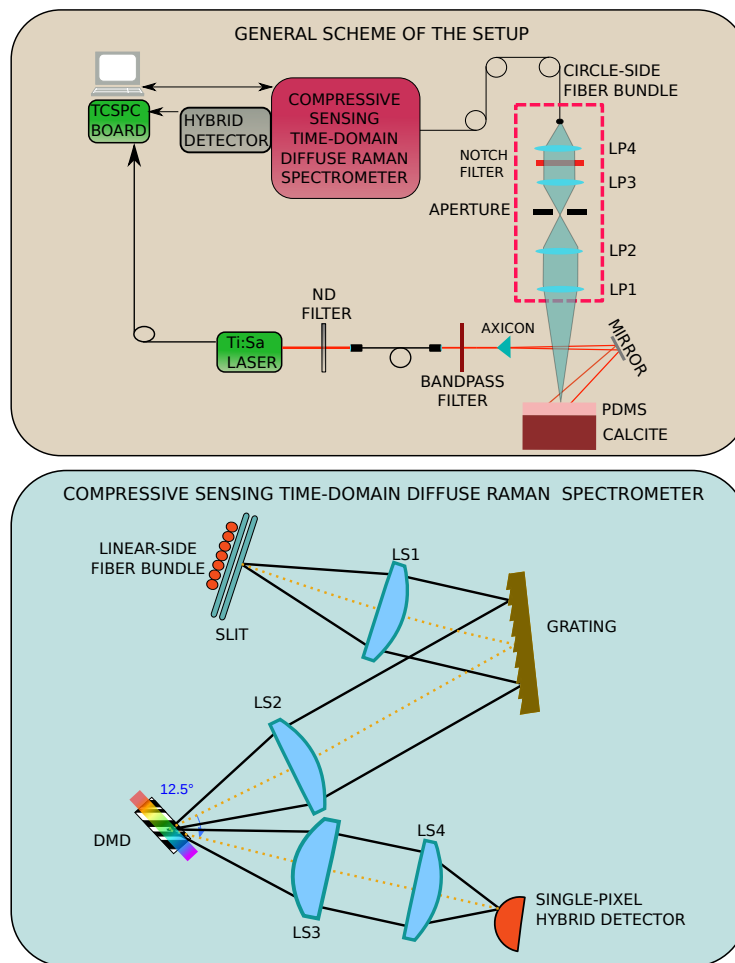


Fig. 1. Schematic representations of the measurement setup. The top panel illustrates the configuration of the measurement setup, highlighting all key components and connections. Probe lenses: LP1 $f = 100$ mm, LP2 $f = 20$ mm, LP3 $f = 25$ mm and LP4 $f = 36$ mm. The bottom panel focuses specifically on the spectrometer setup, providing a detailed depiction of its components and arrangement. TCSPC, Time Correlated Single Photon counting. Spectrometer lenses, LS1 $f = 100$ mm, LS2 $f = 100$ mm, LS3 $f = 100$ mm and LS4 $f = 50$ mm.

Light injection and collection to/from the sample is done with a non-contact probe. On the excitation side, laser light is attenuated via a variable circular attenuator, coupled into a 1 mm core step-index fiber, cleaned by a 10 nm bandpass filter at 780 nm to remove any unwanted spectral component, shaped using an axicon, and finally projected onto the sample to form a circular illumination. Changing the distance between the axicon and the focusing mirror permits to vary the ring radius (from 4 mm up to 10 mm) with thickness of 2 mm.

On the detection side, diffused light is collected from the center of the illuminated ring and coupled to a round-to-line optical fiber with seven cores of 200 μm with a numerical aperture of 0.2 by means of an optical system made of four 1-inch lenses that makes the image of the sample with a lateral magnification factor of 2.2. The first lens (LP1, $f_{LP1} = 100$ mm) and the second lens (LP2, $f_{LP2} = 25$ mm) provide an intermediate image plane where a field stop prevents stray light from entering the detection system. The third lens (LP3, $f_{LP3} = 20$ mm) collimates the light to a 785 nm notch filter with a band of 33 nm (NF785-33, Thorlabs) that removes the elastically scattered light. Finally, the fourth lens (LP4, $f_{LP4} = 36$ mm) makes the image of the collection area on the tip of the fiber bundle.

In Time Domain Diffuse Raman, the average depth reached by photons is encoded into time. Hence, the signal can be collected at a fixed source detection separation ρ . It could be possible to measure at $\rho = 0$ to maximize the photon counts. However, the diffuse optical approximations are not fully verified, making the reconstruction of the individual layer Raman spectra more challenging. Moreover, working at a higher ρ reduces the light intensity from the top layer and increases the photon ratio from the bottom layer. We opted for a source-detector separation of 6 mm.

The optical scheme of the spectrometer is presented in Fig. 1 (bottom). We first placed a 100 μm slit, which is narrower than the fiber core, to improve the spectral resolution at a cost of the optical efficiency. We used 2-inch lenses to obtain a spectrometer with a numerical aperture of 0.25. The 100 mm focal length lens LS1 collimates light from the entrance slit onto the dispersion grating with 1200 lines/mm. The grating separates the light into the wavelength components. We selected the first order of dispersion. A second 100 mm focal length lens LS2 projects the image of the slit onto a DMD (DLP 6500, Texas Instruments) with a magnification factor of 1. The DMD consists of a 1920×1080 micro-mirror matrix that assumes two positions: $+12^\circ$ or -12° . The DMD has a size of 14 mm \times 8 mm, with each mirror having a dimension of 7.6 μm . A homemade program was developed to control the position of the mirrors. Photons reflected by the mirrors at an angle of $+12^\circ$ are sent to the detector. Otherwise, they are removed. Thus, it is possible to filter the collected signal with a binary encoding of $0s$ (remove photons) and $1s$ (collect photons) with any given pattern. The DMD dimension perpendicular to the light dispersion was binned together to increase the photon count since it carries no spectral information. In principle, it could be used to attenuate the signal at wavelengths which could saturate the detector, but this is rarely the case with spontaneous Raman signals. The modulated light is sent to a pair of lenses (LS3, $f_{LS3} = 100$ mm, LS4, $f_{LS4} = 50$ mm) that focuses light with a magnification factor of 0.5 onto a single pixel hybrid detector (HPM100-50, Hamamatsu, Japan) with dimensions of 3 mm \times 3 mm. The detector has a spectral coverage from 400 nm to 900 nm (quantum efficiency: 15% @ 600 nm and \approx 12% @ 800 nm), with a low dark count rate of 200 cps. A Time-Correlated Single-Photon Counting board (TCSPC) was used to process the flow of detected photons and generate the histogram of photon arrival times. The DMD sends a trigger signal to the TCSPC board every time the pattern changes to distinguish the basis vectors. Once the board receives the trigger, it starts a new recording.

2.2. Samples

To study the depth sectioning capabilities of our system, we used a bilayer geometry composed of a 10 mm top layer of silicone elastomer (PDMS) over a 2 cm thick block of calcium carbonate at

the bottom, which will be referred also as calcite. For the top layer, we prepared the PDMS slab by addings 127.6 mg of TiO₂ powder and 7.7 mg of black toner to 128 g of Silicone Elastomer Sylgard 184, resulting in a reduced scattering coefficient, $\mu'_s = 10 \text{ cm}^{-1}$ and an absorption coefficient, $\mu_a = 0.10 \text{ cm}^{-1}$ at 690 nm to mimic typical properties of biological tissues (e.g. skin/adipose tissue layer), whereas we used calcium carbonate to simulate bone. Details on the PDMS phantom preparation are reported in Ref. [24].

To study how autofluorescence from biological samples can affect a measurement on our system, we used a bilayer sample composed of a 10 mm slice of porcine loin over the same block of calcium carbonate presented before. The optical properties of the porcine muscle were measured with a broadband time-domain diffuse optical spectrometer resulting in $\mu'_s = 3 \text{ cm}^{-1}$ and $\mu_a = 0.2 \text{ cm}^{-1}$ at 750 nm.

2.3. Retrieval of Raman spectra

The modulation of the wavelength is performed by the DMD. The light modulation does not affect the distribution of time of flights (DTOF) for the photons at different wavelengths. By considering \mathbf{S}_{wl} to be the actual spectrum matrix and \mathbf{S}_M to be the measured matrix, they can be expressed as:

$$\mathbf{S}_{wl} = \begin{bmatrix} \mathbf{s}_{wl,1} \\ \mathbf{s}_{wl,2} \\ \vdots \\ \mathbf{s}_{wl,n} \end{bmatrix}, \quad \mathbf{S}_M = \begin{bmatrix} \mathbf{s}_{M,1} \\ \mathbf{s}_{M,2} \\ \vdots \\ \mathbf{s}_{M,n} \end{bmatrix}$$

The vectors $\mathbf{s}_{wl,i}$ are the DTOFs across the different wavelengths, while $\mathbf{s}_{M,i}$ are the DTOFs measured over the modulated basis vectors. The modulation can be represented mathematically by the linear system:

$$\mathbf{S}_M = \mathbf{M}\mathbf{S}_{wl} \quad (1)$$

Here, \mathbf{M} is the modulation matrix, typically it is a Hadamard matrix. \mathbf{M} performs the transformation from the wavelength set into the measurement set. The elements of \mathbf{M} are binaries that encode information about the wavelength collection-rejection as $1s$ or $0s$.

According to Ref. [21], we generate the pattern on the DMD used to measure $\mathbf{s}_{M,i}$, by projecting the i^{th} row of the matrix \mathbf{M} onto the DMD's dispersion direction of the wavelength and repeating the values over the perpendicular degenerate direction. This process forms a stripe image on the DMD.

The mode of operation of the spectrometer depends on the basis set uploaded to the DMD. There are two primary choices: monochromator or multiplex mode. Using the monochromator scan the DMD shows a single line at each step, and collects a single wavelength at a time. In this case, in [Eq. (1)], \mathbf{M} is the identity matrix. Conversely, in the multiplex approach, it sends multiple wavelengths to the detector at a time using the Hadamard basis set. In this case, in [Eq. (1)], \mathbf{M} is the Hadamard matrix \mathbf{H} .

The Raman spectrum \mathbf{S}_{wl} for the whole sample is reconstructed in post-processing by solving the linear system:

$$\mathbf{S}_{wl} = \mathbf{M}^{-1}\mathbf{S}_M \quad (2)$$

Using the Hadamard scan, the emitted Raman signal is sampled with a duty cycle of 50% of the time – corresponding to the 50% *on-off* factor of the Hadamard pattern. Conversely, for the monochromator mode only a $1/n$ duty cycle is obtained, where n is the number of lines activated sequentially on the DMD. The Hadamard approach can collect significantly more photons than the monochromator mode, reducing the tradeoff between resolution and integration time.

2.4. Inverse problem

The forward model of the Raman scattering in diffusive media – i.e. the generation of theoretical diffuse Raman time-of-flight – is based on Ref. [25] in which an analytical description of Raman propagation in a diffusive medium deriving from the Diffusion Equation is presented. The inverse problem – i.e. the reconstruction of Raman spectra in heterogeneous media from measurements – is presented in Ref. [20] where a two layer reconstruction is demonstrated. In a bilayer geometry, given the thickness of the two materials and optical parameters, we can express the backscattered signal of Raman photons as the superposition of the diffuse Raman emission from the top (W_{top}) and bottom (W_{bottom}) layers. We assume the same approximation of Ref. [25], that we will refer as heuristic approximation, which consists in modelling the propagation of light as if both photons at excitation and Raman wavelengths see the same optical properties ($\mu_{a,Raman} = \mu_a$ and $\mu'_{s,Raman} = \mu'_s$). Thus, the Raman fluence Φ_e can be expressed with a dependence only on the fluence of the probing light Φ , the speed of light in the tissue v and the time t as $\Phi_e = \Phi - \Phi \exp(-\mu_R vt)$. Since μ_R is extremely low, the previous expression can be further reduced to $\Phi_e \approx \Phi \mu_R vt$ [25]. Considering Fick's law, the reflectance of the surface can be calculated as $R(t) = -D \frac{\partial \Phi}{\partial z}$. The Raman impulse response (W_{top} and W_{bottom}) of each layer is finally the product of two factors: the reflectance of the probing light $R(t)$ and the average pathlength covered by photons in each of the two layers $\langle l_i \rangle = v_i \langle t_i \rangle$ [20], where v_i is the speed of light and $\langle t_i \rangle$ is the average time a photon has travelled inside the layer i .

$$W_{top}(t) = R(t)v_{top}\langle t_{top} \rangle \quad W_{bottom}(t) = R(t)v_{bottom}\langle t_{bottom} \rangle \quad (3)$$

In principle, W_i could be functions of λ , but following the heuristic approximation the Raman impulse response is wavelength independent. The forward model is equal to

$$\mathbf{I}(\lambda) = [W_{top} W_{bottom}] \begin{bmatrix} \mu_{R,top}(\lambda) \\ \mu_{R,bottom}(\lambda) \end{bmatrix} \quad (4)$$

where I is the ideal distribution of Raman photons, and $\mu_{R,top}$, $\mu_{R,bottom}$ are the Raman scattering coefficients for the top and bottom layers, respectively.

In the real scenario, the non-ideal spectrometer's impulse response should be taken into account. Therefore we need to convolve the instrument response function IRF to the ideal response of the sample:

$$\mathbf{M}(\lambda) = A (IRF * \mathbf{I}(\lambda)) = A \cdot IRF * [W_{top} W_{bottom}] \begin{bmatrix} \mu_{R,top}(\lambda) \\ \mu_{R,bottom}(\lambda) \end{bmatrix} \quad (5)$$

where A is a constant amplitude accounting for the overall efficiency, including the laser power, the collection optics, the spectrometer, and the detector.

Since the spectrometer was designed to remove the probing light, it is not possible to directly measure the IRF of the system. We can extrapolate the IRF using one Raman peak. We know that:

$$M_i = A \mu_{R,i} IRF * W_i \quad (6)$$

Using the normalised signal of the top layer (PDMS) M_{top} presented in Fig. 6 (left) and the theoretical W_{top} , we infer from [Eq. (6)] the FWHM and time t_0 of the impulse by assuming $IRF(t) = \exp(-(t - t_0)^2 / \sigma) * \exp(-t/\tau)$, where a Gaussian temporal profile is typical of lasers and the exponential decay is typical of hybrid detectors. We assume the τ parameter to be intrinsic to the detector and was obtained by fitting this theoretical IRF with the one presented in Fig. 2 (left). This procedure for IRF estimate is justifiable given the easy accessibility of the top layer in practical cases.

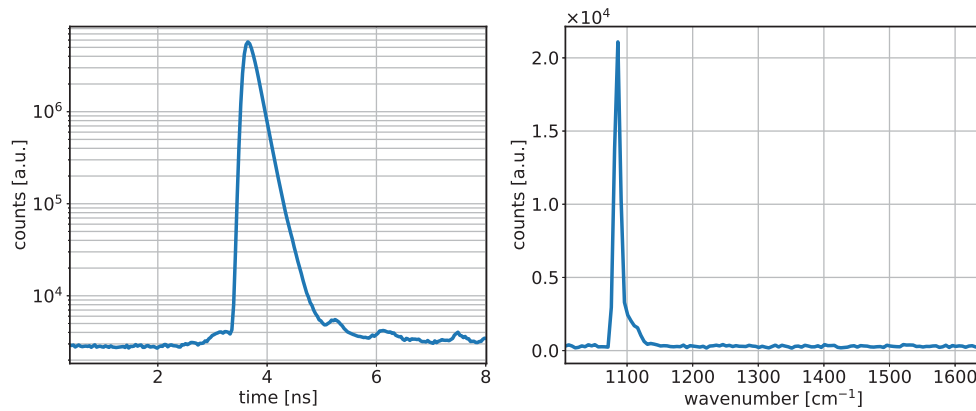


Fig. 2. Temporal (left) and spectral (right) resolution analysis of the time-domain diffuse Raman spectrometer, utilizing an excitation wavelength of 852 nm. The measured temporal FWHM is 280 ps, while the spectral FWHM is 11 cm⁻¹.

After estimating the IRF, we can solve the linear system [Eq. (5)] to obtain $A\mu_{R,top}$ and $A\mu_{R,bottom}$. For simplicity, we denote these values as $\mu'_{R,top}$ and $\mu'_{R,bottom}$, respectively, and refer to them as the relative Raman scattering coefficients. For clarity we can normalize by dividing them by the maximum value of $\mu'_{R,top}(\lambda)$.

3. System characterisation

The diffuse Raman spectrometer was characterised in terms of spectral resolution, spectral range, temporal resolution and optical efficiency. The spectrometer specifications are shown in Table 1.

To measure the *spectral resolution*, we changed the wavelength of the laser to 852 nm, which is within the spectral range of the spectrometer. Laser light was collected by the bundle of fibers after passing through a diffusive medium to excite all modes and cores in the fiber as in a real measurement on a turbid medium. The resulting *spectral resolution* is 0.8 nm or 11 cm⁻¹ full width at half maximum (FWHM) at 852 nm, as shown in Fig. 2 (right). The DMD can show up to 256 patterns, enabling us to collect 256 temporal profiles, each corresponding to a different basis projection. The spectrometer resolution is currently limited by the dimension of the image of the fiber on the DMD plane. To probe the limits of the system we used a small, single mode fiber (core 3 μm), reaching a resolution of 0.2 nm or 3 cm⁻¹, which can be considered as the ultimate spectral resolution of the spectrometer.

The *spectral range* of the spectrometer is 50 nm or 700 cm⁻¹ using 780 nm as the excitation wavelength, estimated by tuning the laser excitation wavelength. This range is adequate considering that it covers more than half of the Raman fingerprint region (450 - 1550 cm⁻¹). We performed a first coarse spectral calibration of the spectrometer tuning the laser excitation wavelength and a reference spectrometer (USB2000 from Ocean Optics) and fine-tuned using two reference peaks, one from silicone and one from calcium carbonate.

The *temporal resolution* is measured by directly connecting the laser output to the seven-core fiber. We excite all the fiber modes by adding a piece of Teflon at the connection of the 1 mm fiber to the seven-core fiber. Propagation through a diffusive sample is not applicable here since it would broaden the temporal pulse. The temporal resolution of the spectrometer is 280 ps (FWHM), as shown in Fig. 2 (left). The elements that influence the temporal resolution of the system are the laser pulse, fiber broadening, broadening in the spectrometer and detector response.

The *optical efficiency* of the spectrometer was measured using a radiometer (THORLABS, S140C Power Sensor) by taking the ratio of the power reaching the detector plane over the total power of the laser. The *optical efficiency* of the spectrometer is 4% at 850 nm. The photon loss of the spectrometer is caused by different orders of the grating, lenses, the fill factor of the DMD, and the slit width. The total efficiency of the spectrometer is $\approx 1\%$, accounting also for the quantum efficiency of the detector.

4. Diffuse Raman measurements on tissue equivalent phantoms

To validate the system, we measured two materials with well defined Raman emission, namely PDMS and calcium carbonate. The reference spectra, collected with a commercial system, are presented in Fig. 3 for PDMS (left) and calcium carbonate (right). Calcium carbonate has an intense signal at 1086 cm^{-1} . PDMS has a much weaker Raman intensity compared to calcium carbonate, with two main peaks at 1411 cm^{-1} and 1260 cm^{-1} .

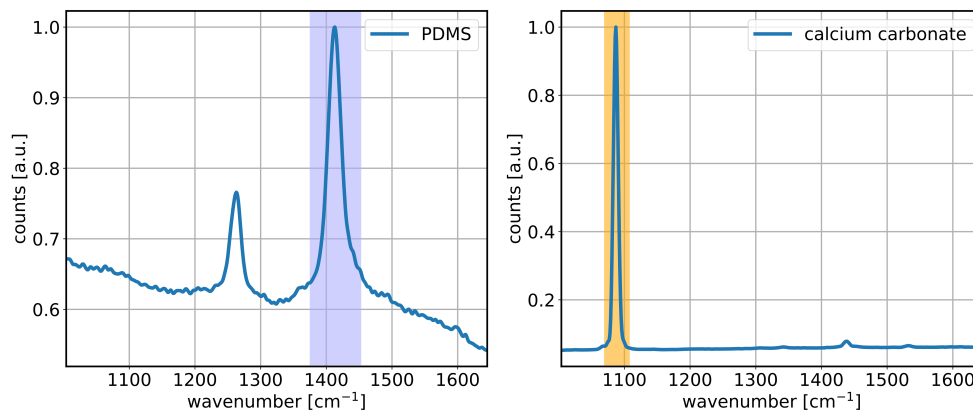


Fig. 3. Reference spectra of calcium carbonate (right) and PDMS (left). The Raman spectrum was obtained using a confocal microscope (X73, Olympus Europa SE & Co. KG, Hamburg, Germany) equipped with an excitation wavelength of 660 nm and the collected light coupled to a spectrometer (Isoplane160, Princeton Instruments, Trenton, NJ, USA) with a 600 lines/mm grating and a CCD sensor (PIXIS256F, Princeton Instruments, Trenton, NJ, USA).

Table 1. System specification

Fundamental spectra resolution	11 cm^{-1}
Temporal resolution	276 ps
f-number	1.96
NA	0.25
slit-size	$100\ \mu\text{m}$
number of elements	256
optical efficiency	4%

To challenge the system on Diffuse Raman measurements, we used a tissue-mimicking phantom composed of a 1 cm top layer of silicone with optical properties similar to fat tissue, overlying a block of calcium carbonate – mimicking bone.

The measurements were performed at 780 nm with 100 mW and we collected using 128 patterns with a source detection separation of 6 mm. The integration time for every base vector was 12 s. The total integration time was 1536 s (≈ 25.5 minutes).

We performed the measurement using two modalities: monochromator mode or Hadamard mode. The difference between these two modes is the basis set shown on the DMD as explained in section 2.3. The monochromator mode uses the trivial basis set where one line corresponds to a wavenumber. The Hadamard mode measures on a more complex set requiring the reconstruction onto the wavelength basis.

As proof of the advantage in harvesting efficiency of the Hadamard mode, in Fig. 4 we show the resulting spectra obtained using the two different modalities with the very same total acquisition time (25.5 min), by integrating over the photon arrival time, equivalently to a standard continuous wave (CW) Diffuse Raman measurement as in SORS.

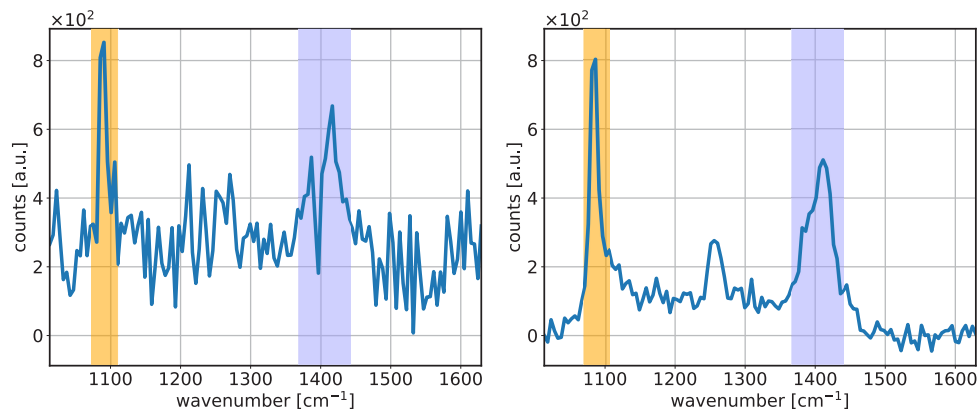


Fig. 4. Comparison of Raman spectra obtained using the monochromator mode (left) and Hadamard mode (right), employing identical integration times. Notably, the Hadamard mode exhibits significantly reduced noise levels compared to the traditional monochromator approach, enhancing the overall data quality.

The Hadamard spectrum is significantly less noisy compared to the monochromator spectrum. This is due to the Hadamard mode collecting 57 times more photons than the monochromator mode, with a count of 2,100,000 photons compared to 37,000 photons. Signal harvesting is notably a key issue for Raman spectroscopy, but even more for DIRS due to the additional attenuation caused by light propagation in the diffusive medium. From the CW measurement in Fig. 4 we can recognize three strong peaks at 1086 cm^{-1} , 1411 cm^{-1} , and a smaller one at 1260 cm^{-1} , which, compared with the reference spectra in Fig. 3, can be certainly attributed to calcium carbonate (the first one) and to PDMS (the latter two). However, it is impossible to distinguish the depth origin of the Raman peaks from a CW measurement alone. For this purpose, we have to look at the photons' arrival time. The complete measurement is presented in a 2D plot in Fig. 5 (left) where the wavenumber is presented on the x-axis, the time in ps on the y-axis and the photon count at each time-gate of a single wavenumber is color-coded. In some time-gates, we observe a negative photon count, which is an artifact introduced by the Hadamard reconstruction. In Fig. 5 (left) three strong signals are again recognizable. We observe that the stripe at 1086 cm^{-1} is delayed as compared to the other two. This signal comes from the Raman photons emitted by the marble layer at 1 cm depth. To better visualize the time delay and appreciate the depth probing capabilities of time, in Fig. 5 (right) we bin the measurement in 8 adjacent time-windows of 270 ps width and plot the spectra at each time gate. In the first gate we show photons that arrive at a time lower than 270 ps and we can measure only Raman photons

with 1411 cm^{-1} and 1260 cm^{-1} . Those photons are the Raman signature of PDMS and they come from the top layer. In the second time-gate, we observe the slow rise of the signal at 1086 cm^{-1} . It is the Raman signature of calcium carbonate of the bottom layer. In the fourth gate, it is possible to observe the maximum intensity of the calcium carbonate peak and see that the silicone photons are nearly extinguished. In the following gates, the Raman signal of the calcium carbonate also slowly decreases. Although a direct correlation between photons time-of-flight and signal depth in diffuse Raman is not yet available in literature, we can consider valid, as a first approximation, the results of Ref. [26] about this correlation in diffuse optics. Thus, we can associate to the first time gate an average depth of 3 mm, to the second time gate 5 mm and to the fourth and fifth time gate, where the signal from the bottom layer is prevalent, depths of 7 mm and 9 mm. The average depth of 10 mm is reached in the last time gate where, in fact, almost only the signal from the bottom layer is present.

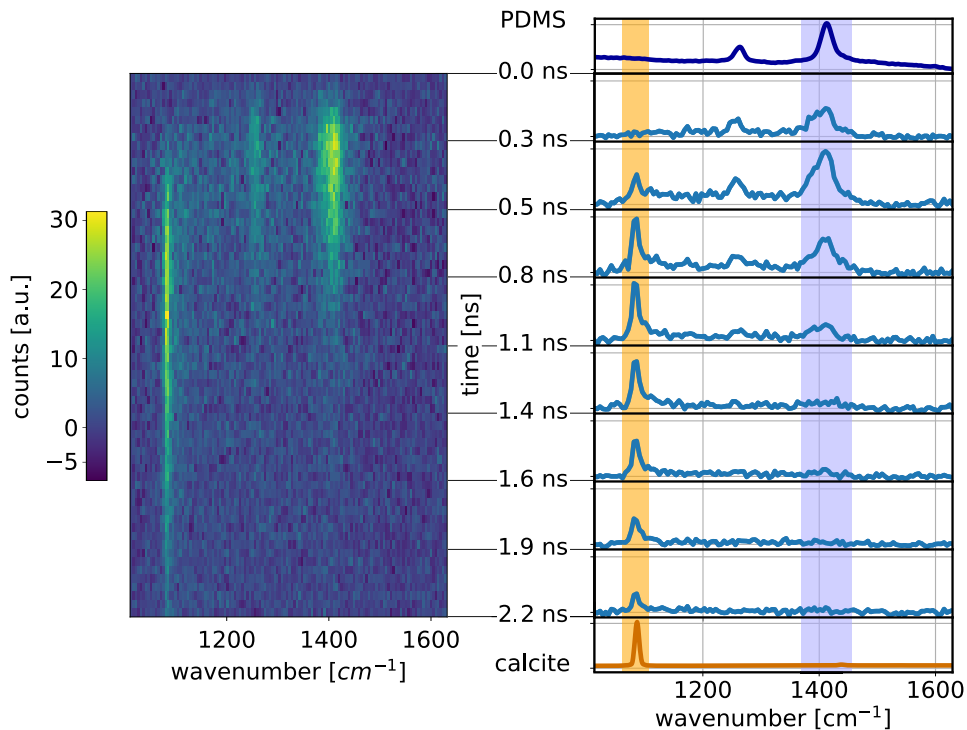


Fig. 5. Temporal evolution of Raman spectra of the PDMS-calcite phantom. The left panel illustrates the evolution using a colormap, while the right panel displays the spectra at different time-gates. The Raman signal of calcium carbonate (orange) at 1086 cm^{-1} arrives later than the PDMS signal (blue) at 1411 cm^{-1} , indicating a delayed response of the calcium carbonate component.

Signals arising from the two layers have different temporal evolution. To better appreciate this effect, Fig. 6 (left) displays the temporal distribution of photon arrival times related to the 1411 cm^{-1} peak – superficial layer (blue line) – and the 1086 cm^{-1} peak – deep layer (orange line). The curves were obtained by slicing the reconstructed 2D spectra over two spectral windows centered on the respective peaks. The broader and time-shifted temporal distribution of the orange curve is suggestive of a deeper-arising signal.

We extend the concept of the enhancement factor presented in Ref. [14] for FORS and SORS to the time-domain. The enhancement factor seeks to obtain a metric independent of the Raman strength of the material to grade the capability to separate the deep-layer Raman signal from the

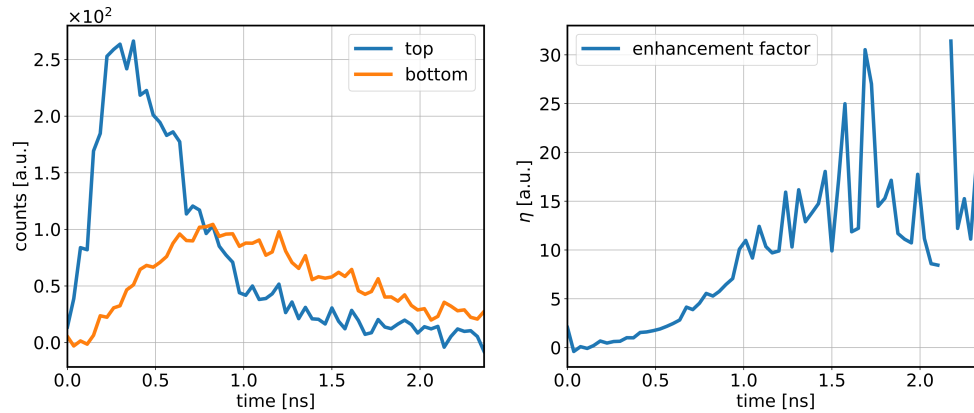


Fig. 6. The left panel presents the temporal evolution of the Raman signal for both the top layer (PDMS) and bottom layer (calcium carbonate). The Raman photons originating from the bottom layer exhibit a noticeable delay compared to those from the top layer due to the additional travel path through the first layer. On the right, the calculated enhancement factor is depicted, showcasing a smooth profile until 1 ns and subsequently displaying increased noise at later times due to the extremely low photon counts from the top layer.

superficial one. We defined the enhancement factor in TD-DIRS as:

$$\eta = \frac{\frac{I_{bottom}(t)}{I_{top}(t)}}{\frac{I_{bottom}(t_0)}{I_{top}(t_0)}} \quad (7)$$

where $I(t)$ stands for the signal intensity collected from either the bottom (i.e. 1086 cm^{-1} peak) or top (i.e. 1411 cm^{-1} peak) layer at a generic photon arrival time t , while t_0 is a reference temporal position for intensity normalization. The time t_0 is taken at the position of the maximum of the signal from the top layer. The resulting enhancement factor is shown in Fig. 6 (right).

The photons from the bottom layer in the later gates reach an enhancement factor of 25. However, after 1500 ps the S/N ratio of the photons from the top layer is too low to provide reliable data.

Using the Porcine-calcium carbonate phantom sample presented in section 2.2, we studied the feasibility of this spectrometer on biological samples to detect Raman photons at depth. The measurement was performed at 780 nm with 500 mW using 128 patterns and a source detection separation of 6 mm. The total integration time was 1 hour and the integration time for each pattern was 28 s. The results is shown in Fig. 7. This measurement shows that, in a biological sample, there is a significant presence of autofluorescence which gives a uniform background over the whole spectral range. The bell-shaped structure of the measured spectrum is due to different wavelength efficiency caused by a vignetting effect in the spectrometer. By time gating the spectra and selecting late gates corresponding to signal from deep layers, we can reject the autofluorescence originating in the first layer composed of porcine muscle and observe the appearance of the calcium carbonate Raman peak of the bottom layer. This demonstrates that, although diffuse Raman measurements of biological materials have an important contribution of autofluorescence, it is feasible to retrieve a Raman spectrum from depth in a biological sample opening the possibility to *ex vivo* and *in vivo* applications.

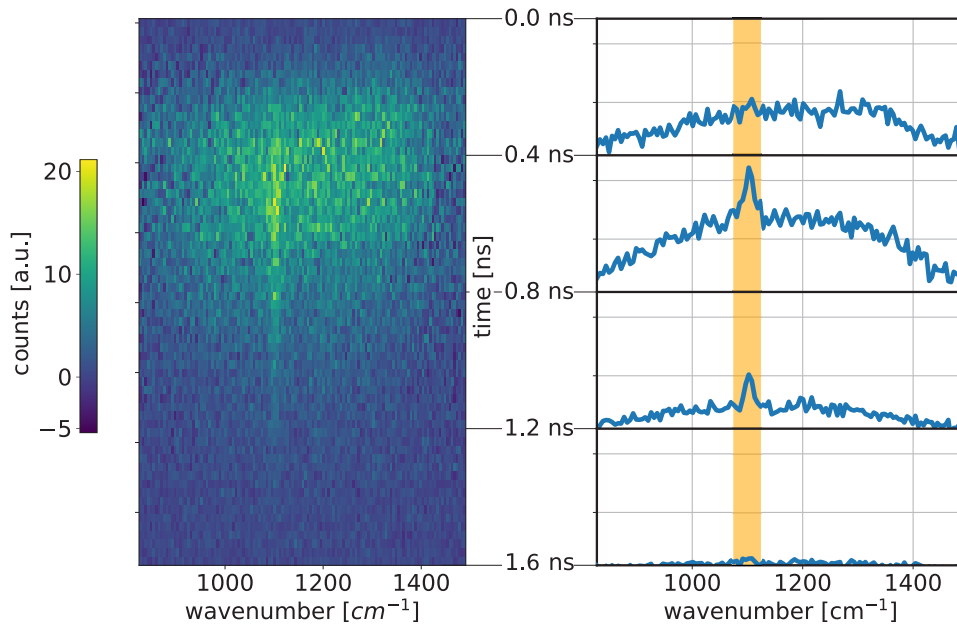


Fig. 7. Temporal evolution of Raman spectra of the porcine loin-calcite phantom. The left panel illustrates the evolution using a colormap, while the right panel displays the spectra at different time-gates. The Raman signal of calcium carbonate (orange) at 1086 cm^{-1} is barely visible because of autofluorescence over the whole spectral range. Only in late time gates we can distinguish the peak from the background.

5. Two-layer reconstruction

In the previous section, we presented the results of our experiments and highlighted the relationship between time and depth. However, we want also to reconstruct the relative Raman scattering coefficient of each layer separately. To obtain the reconstruction of the spectra of the two layers we need several parameters of both layers: the refractive index, the absorption coefficient, the reduced scattering coefficient and the thickness of the two layers. The absorption and reduced scattering coefficients for both PDMS and calcium carbonate were roughly estimated due to the heuristic approximation that assume the optical properties are the same all over the spectra. In reality, the optical properties differ between the Raman and excitation wavelengths. Using a broadband time-domain diffuse optical spectrometer, the coefficients μ_a and μ'_s were measured as shown in Ref. [24]. For PDMS, they were approximated to be $\mu_a = 0.1\text{ cm}^{-1}$ and $\mu'_s = 9\text{ cm}^{-1}$, while for calcium carbonate, they were approximated to be $\mu_a = 0.1\text{ cm}^{-1}$ and $\mu'_s = 10\text{ cm}^{-1}$.

In Fig. 8 we present the reconstruction of the spectra for the two layers based on the model described in section 2.4. The relative Raman scattering coefficient μ'_R shown has been normalized for clarity, by dividing the spectra with the maximum value from $\mu'_{R,top}$ therefore in Fig. 8 it has been shown in arbitrary units. The total computation time for the two-layer reconstruction was 2.2 s on an Intel i5-1135G7 processor.

We observe the separation of the relative Raman scattering coefficient of the bottom layer from the one from the top. In the top layer reconstruction, we notice a small peak at 1086 cm^{-1} in correspondence to the Raman peak of calcium carbonate of the bottom layer. This small cross-talk could be ascribed to the uncertainties in the measurement of the IRF, in the measurements of the optical parameters or any issues with the model caused by the diffusion approximation. The reconstruction method offers several key advantages over the time-gated method. Firstly,

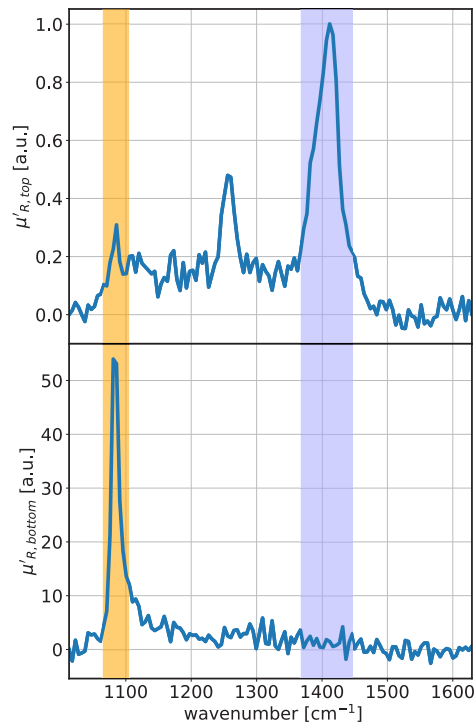


Fig. 8. Reconstruction of the relative Raman scattering coefficient for the two layers, with the intensity normalized to the maximum value of the top layer.

it provides an improved separation between the spectra of different layers. This enhanced spectral resolution allows for a more accurate characterization and analysis of individual layer contributions. Secondly, it obtains a quantity that is related to the Raman scattering coefficient by a constant. Traditional Raman spectra are influenced by the optical properties (μ_a and μ'_s) of the materials. Consequently, the intensity measured in such spectra cannot be readily interpreted as a quantitative measure. By utilizing the reconstruction method, it becomes possible to obtain a quantity proportional to the Raman scattering coefficients that provide an estimate of the chemical composition as it follows the Beer-Lambert law: $\mu_R = \sum c_i \mu_{R,i}$, where μ_R is the Raman scattering coefficient, c_i is the molar concentration of a molecule and $\mu_{R,i}$ is the molar Raman coefficient.

6. Conclusion

In this work, we presented an innovative Time-Domain Diffuse Raman spectrometer that uses a single pixel detector and exploits a DMD for encoding the wavelengths, following the design proposed by Ref. [21]. It overcomes the main limitation of alternative TD-DIRS systems, based on either expensive and spectrally limited [14] or more noisy not-single-photon [17] camera detectors, or on detector arrays with a small number of elements. Using the Hadamard basis set, it is possible to overcome the trade-off between resolution and acquisition time as the duty cycle for each wavelength is 50% compared to $1/n$ for a monochromator scan. We have validated the system on a two-layer tissue-mimicking phantom made of a PDMS slab (1 cm, $\mu_a = 0.1 \text{ cm}^{-1}$, $\mu'_s = 10 \text{ cm}^{-1}$) overlying a calcium carbonate block and proved sensitivity to the Raman signal originating from depth and differentiation of the two layers, with an enhancement factor of 25 between the top and bottom layer signals. We demonstrated the feasibility of obtaining the Raman signal from depth on biological tissue with a two-layer phantom composed of porcine

muscle (1 cm , $\mu_a = 0.2\text{ cm}^{-1}$, $\mu'_s = 3\text{ cm}^{-1}$) overlaying the same calcium carbonate block. Finally, we reconstructed the Raman scattering spectra of the PDMS-calcium carbonate phantom using an inverse model [20] based on the diffusion equation modified using a heuristic approximation. Work is now in progress to apply this novel approach of TD-DIRS spectroscopy in both *ex vivo* and *in vivo* studies, with a focus on biomedical applications.

Funding. Ministero dell'Università e della Ricerca (D2B8D520, 2020WMSNBL, 2022598YAX, 2022EB4B7E).

Acknowledgments. We acknowledge support from the Italian Ministry of University and Research PRIN projects: Grant No. 2020WMSNBL, Grant No. 2022EB4B7E; Grant No. 2022598YAX, and from the European Union's NextGenerationEU Programme with the I-PHOQS Infrastructure [IR0000016, ID D2B8D520, CUP B53C22001750006]. We also want to thank Marco Ventura for providing the reference Raman spectra.

Disclosures. The authors declare no potential conflicts of interest.

Data Availability. The data that support the findings of this study are available from the corresponding author, A.B., upon reasonable request.

References

1. S. Mosca, P. Dey, M. Salimi, B. Gardner, F. Palombo, N. Stone, and P. Matousek, "Spatially Offset Raman Spectroscopy - How Deep?" *Anal. Chem.* **93**(17), 6755–6762 (2021).
2. N. Stone, R. Baker, K. Rogers, A. W. Parker, and P. Matousek, "Subsurface probing of calcifications with spatially offset Raman spectroscopy (SORS): Future possibilities for the diagnosis of breast cancer," *Analyst* **132**(9), 899–905 (2007).
3. N. Stone and P. Matousek, "Advanced transmission Raman spectroscopy: A promising tool for breast disease diagnosis," *Cancer Res.* **68**(11), 4424–4430 (2008).
4. M. Dooley, J. McLaren, F. R. Rose, and I. Notingher, "Investigating the feasibility of spatially offset Raman spectroscopy for in-vivo monitoring of bone healing in rat calvarial defect models," *J. Biophotonics* **13**(10), e202000190 (2020).
5. C. Conti, A. Botteon, C. Colombo, D. Pinna, M. Realini, and P. Matousek, "Advances in Raman spectroscopy for the non-destructive subsurface analysis of artworks: Micro-SORS," (2020).
6. A. Botteon, C. Conti, M. Realini, C. Colombo, and P. Matousek, "Discovering Hidden Painted Images: Subsurface Imaging Using Microscale Spatially Offset Raman Spectroscopy," *Anal. Chem.* **89**(1), 792–798 (2017).
7. J. Qin, K. Chao, and M. S. Kim, "Investigation of Raman chemical imaging for detection of lycopene changes in tomatoes during postharvest ripening," *J. Food Eng.* **107**(3–4), 277–288 (2011).
8. C. Eliasson and P. Matousek, "Noninvasive authentication of pharmaceutical products through packaging using spatially offset Raman spectroscopy," *Anal. Chem.* **79**(4), 1696–1701 (2007).
9. B. Cletus, W. Olds, P. M. Fredericks, E. Jaatinen, and E. L. Izake, "Real-time detection of concealed chemical hazards under ambient light conditions using Raman spectroscopy," *J. Forensic Sci.* **58**(4), 1008–1014 (2013).
10. C. Eliasson, N. A. Macleod, and P. Matousek, "Non-invasive detection of powders concealed within diffusely scattering plastic containers," *Vib. Spectrosc.* **48**(1), 8–11 (2008).
11. S. Mosca, C. Conti, N. Stone, and P. Matousek, "Spatially offset Raman spectroscopy," *Nat. Rev. Methods Primers* **1**(1), 21 (2021).
12. P. Matousek, I. P. Clark, E. R. C. Draper, M. D. Morris, A. E. Goodship, N. Everall, M. Towrie, W. F. Finney, and A. W. Parker, "Subsurface Probing in Diffusely Scattering Media Using Spatially Offset Raman Spectroscopy," *Tech. Rep.* 4 (2005).
13. P. Matousek and A. W. Parker, "Bulk Raman analysis of pharmaceutical tablets," *Appl. Spectrosc.* **60**(12), 1353–1357 (2006).
14. S. K. V. Sekar, S. Mosca, A. Farina, F. Martelli, P. Taroni, G. Valentini, R. Cubeddu, and A. Pifferi, "Frequency offset Raman spectroscopy (FORS) for depth probing of diffusive media," *Opt. Express* **25**(5), 4585 (2017).
15. S. Konugolu Venkata Sekar, S. Mosca, S. Tannert, G. Valentini, F. Martelli, T. Binzoni, Y. Prokazov, E. Turbin, W. Zuschratter, R. Erdmann, and A. Pifferi, "Time domain diffuse Raman spectrometer based on a TCSPC camera for the depth analysis of diffusive media," *Opt. Lett.* **43**(9), 2134 (2018).
16. A. Torricelli, A. Pifferi, L. Spinelli, R. Cubeddu, F. Martelli, S. Del Bianco, and G. Zaccanti, "Time-resolved reflectance at null source-detector separation: Improving contrast and resolution in diffuse optical imaging," *Phys. Rev. Lett.* **95**(7), 078101 (2005).
17. F. Ariese, H. Meuzelaar, M. M. Kersters, J. B. Buijs, and C. Gooijer, "Picosecond Raman spectroscopy with a fast intensified CCD camera for depth analysis of diffusely scattering media," *Analyst* **134**(6), 1192–1197 (2009).
18. M. Kögler and B. Heilala, "Time-gated Raman spectroscopy – a review," *Meas. Sci. Technol.* **32**(1), 012002 (2020).
19. J. Kekkonen, J. Nissinen, and I. Nissinen, "Depth Analysis of Semi-Transparent Media by a Time-Correlated CMOS SPAD Line Sensor-Based Depth-Resolving Raman Spectrometer," *IEEE Sens. J.* **19**(16), 6711–6720 (2019).
20. S. Šušnjar, F. Martelli, S. Mosca, V. Konugolu, S. Sekar, J. Swartling, N. Reistad, A. Farina, and A. Pifferi, "Two-layer reconstruction of Raman spectra in diffusive media based on analytical model in the time domain," *preprints opticaopen* (2023).

21. P. Berto, C. Scotté, F. Galland, H. Rigneault, and H. B. de Aguiar, "Programmable single-pixel-based broadband stimulated Raman scattering," *Opt. Lett.* **42**(9), 1696 (2017).
22. M. Pagliuzzi, S. K. V. Sekar, L. Colombo, E. Martinenghi, J. Minnema, R. Erdmann, D. Contini, A. D. Mora, A. Torricelli, A. Pifferi, and T. Durduran, "Time domain diffuse correlation spectroscopy with a high coherence pulsed source: in vivo and phantom results," *Biomed. Opt. Express* **8**(11), 5311 (2017).
23. S. Samaei, L. Colombo, D. Borycki, M. Pagliuzzi, T. Durduran, P. Sawosz, S. Wojtkiewicz, D. Contini, A. Torricelli, A. Pifferi, and A. Liebert, "Performance assessment of laser sources for time-domain diffuse correlation spectroscopy," *Biomed. Opt. Express* **12**(9), 5351 (2021).
24. F. Zhao, P. Levoni, L. Frabasile, H. Qi, M. Lacerenza, P. Lanka, A. Torricelli, A. Pifferi, R. Cubeddu, and L. Spinelli, "Reproducibility of identical solid phantoms," *J. Biomed. Opt.* **27**(07), 074713 (2022).
25. F. Martelli, T. Binzoni, S. K. V. Sekar, A. Farina, S. Cavalieri, and A. Pifferi, "Time-domain Raman analytical forward solvers," *Opt. Express* **24**(18), 20382 (2016).
26. F. Martelli, T. Binzoni, A. Pifferi, L. Spinelli, A. Farina, and A. Torricelli, "There's plenty of light at the bottom: Statistics of photon penetration depth in random media," *Sci. Rep.* **6**(1), 27057 (2016).